Fuzzy Droop Control for SOC Balance and Stability Analysis of DC Microgrid with Distributed Energy Storage Systems

Jipeng Gu, Xiaodong Yang, Youbing Zhang, Luyao Xie, Licheng Wang, Wenwei Zhou, and Xiaohui Ge

***Abstract*—The unbalanced state of charge (SOC) of distributed energy storage systems (DESSs) in autonomous DC microgrid causes energy storage units (ESUs) to terminate operation due to overcharge or overdischarge, which severely affects the power quality. In this paper, a fuzzy droop control for SOC balance and stability analysis of DC microgrid with DESSs is proposed to achieve SOC balance in ESUs while maintaining a stable DC bus voltage. First, the charge and discharge modes of ESUs are determined based on the power supply requirements of the DC microgrid. One-dimensional fuzzy logic is then applied to establish the relationship between SOC and the droop coefficient R_d in the aforementioned two modes. In addition, when integrated with voltage-current double closed-loop control, SOC balance in different ESUs is realized. To improve the balance speed and precision, an exponential acceleration factor is added to the input variable of the fuzzy controller. Finally, based on the average model of converter, the system-level stability of microgrid is analyzed. MATLAB/Simulink simulation results verify the effectiveness and rationality of the proposed method.**

***Index Terms*—DC microgrid, distributed energy storage system, fuzzy droop control, state of charge (SOC) balance, stability analysis.**

I. Introduction

DISTRIBUTED generation technology has attracted considerable attention from researchers because of its advantages of environmental friendliness and high energy efficiency. However, when distributed energy resources are directly connected to the existing power system, the probability of power imbalance is increased. Therefore, the concept of a microgrid has been proposed [1]-[3]. Compared with AC microgrid, DC microgrid has the advantages of simple structure, fewer energy conversion links, and low system energy loss. In addition, reactive power and harmonics are not considered [4], [5].

As the output of distributed energy resources such as photovoltaic and wind power is intermittent and random, it is difficult to balance the supply and demand power of the microgrid. In other words, the bus voltage is unstable, which severely affects the output power quality. Therefore, distributed energy storage systems (DESSs) with certain capacities should be configured to absorb or release electrical energy to solve these problems [6]-[8]. Compared with setting a single energy storage unit (ESU), setting multiple ESUs is more conducive to capacity expansion and standardization. However, when multiple ESUs are present in a DESS, if an state of charge (SOC) balance in ESUs cannot be achieved, deep charge and excessive discharge will occur in some ESUs, which will affect the service life of the DESS and stable operation of the microgrid [9]-[11].

The control strategies for rational load power distribution among ESUs include centralized control, decentralized control, and distributed control. Centralized control is performed through a central controller to collect the information related to the integration and processing of each unit following the issuance of control instructions. In [12], the information of rated power and SOC of different ESUs is used to design an energy management system that could monitor and correct relevant variables to ensure power sharing among ESUs in the event of a converter failure and fault crossing in a microgrid. In [13], a master-slave control structure is adopted to achieve SOC balance in ESUs in a DESS. The master controller provides the current reference value for each modular unit while ensuring bus voltage stability and the SOC information to the slave controller to achieve SOC balance. Decentralized control involves the transmission of collected information from each unit to the local controller and implementation of the control, where the main type of control is droop control. In [14], a droop control method is proposed that considers the differences in line impedance, initial SOC, and capacity, which could ensure the bus voltage stability and SOC balance in ESUs. In [15], a quasi-sliding mode cur-

Manuscript received: February 27, 2023; revised: June 14, 2023; accepted: December 12, 2023. Date of CrossCheck: December 12, 2023. Date of online publication: January 2, 2024.

This work was supported by the National Natural Science Foundation of China (No. U22B20116).

J. Gu, Y. Zhang (corresponding author), L. Xie, L. Wang, and W. Zhou are with the College of Information Engineering, Zhejiang University of Technology, Hangzhou 310023, China (e-mail: jipenggu@163.com; youbingzhang@zjut.edu.cn; xieluyao@zjut.edu.cn; wanglicheng@zjut.edu.cn; zww@zjut.edu.cn).

X. Yang is with the College of Electrical Engineering, Hefei University of Technology, Hefei 230006, China (e-mail: yang_xd90@163.com).

X. Ge is with the Electric Power Research Institute of State Grid Zhejiang Electric Power Co., Ltd., Hangzhou 310023, China (e-mail: gegexiaoui@126.com).

DOI: 10.35833/MPCE.2023.000119

rent control strategy based on discrete time is proposed to realize the cooperative operation of energy storage converters and SOC balance in a DESS. In [16] and [17], control methods for SOC exponential and SOC power function droops are proposed, respectively, both of which could ensure the reasonable power distribution of DESS. Distributed control is implemented by adding a communication mechanism based on a local controller [18]. References [16] and [17] show that the relationship between the SOC of each ESU and its corresponding droop coefficient R_{di} can be expressed using a variety of mathematical models. However, it can just as easily be expressed using the fuzzy control rules described by natural language. Fuzzy control is an intelligent control method with good robustness and adaptability and is often combined with traditional control methods to realize the automation of complex systems [19], [20]. Therefore, this paper integrates fuzzy control based on current-voltage droop control (called *I-U* droop control), that is, SOC fuzzy droop control. All the control methods designed in the aforementioned studies can realize the SOC balance in ESUs. However, the research on balance speed is rarely mentioned. Realizing the SOC balance in ESUs in a short time will be more conducive to improving power quality and ensuring the safe and stable operation of microgrid. The SOC fuzzy droop control with acceleration factor proposed in this paper is based on this viewpoint.

Many studies have been conducted on the stability of microgrid that contains a DESS, and various stability analysis methods have been used. The equivalent models and stabilities of DESS are discussed in [21], including an average model that uses an AC voltage source instead of a switch, a DC link model that uses a DC voltage source instead of an energy storage and converter, and a detailed model that includes all components and control circuits. References [22]-[24] establish generalized model, average model, and low-order equivalent model of DESS, respectively. They then study the stable operation areas of microgrid under the conditions of relevant parameter changes based on the aforementioned models. In [25], the small-signal model theory is used to analyze the effects of supercapacitor voltage on system stability in a hybrid energy-storage DC microgrid. In addition, a coordinated control method is proposed to ensure that the microgrid has both a high amplitude margin and phase angle margin. In [26], the Lyapunov method is applied to derive the stability criterion of the DC microgrid drop control form and is compared with the mixed potential energy function to verify the validity of the criterion. Based on various equivalent models of converters such as the average model, small-signal model, and large-signal model, the aforementioned studies apply nonlinear system theory to study the stability of microgrid in terms of time and frequency domains. It is noteworthy that the aforementioned models can be transformed into any of the others. The average model is a continuous-time model by which it is relatively easy to conduct principle analysis and controller design. The model also has strong applicability [27]. Therefore, a stability analysis based on the converter average model is applicable to the design of the microgrid in this paper, but the possibility of using other models cannot be excluded.

A DESS in a DC microgrid can ensure that the energy supply of the system will not fluctuate significantly under load switching, circuit failure, or environmental change. However, it is necessary to consider a reasonable distribution of load power among all ESUs to ensure a consistent SOC and to avoid early withdrawal of some ESUs due to overcharge and overdischarge. These problems are described in [28]-[32]. To realize a fast SOC balance in ESUs in a DC microgrid, an SOC fuzzy drop control method with an acceleration factor is proposed, and the system stability is studied based on the average model of converters. The contributions of this paper are as follows.

1) The relationship between the SOC deviation of each ESU and the corresponding droop coefficient is established through one-dimensional fuzzy logic. The droop coefficient can be automatically adjusted according to the changes in the external environment, which greatly simplifies the complexity of the system control structure.

2) When the SOC of the ESUs tends to be consistent, an exponential acceleration factor is added, which improves the balance speed and precision to a certain extent.

3) Based on the average model theory, the frequency domain stability of a DC microgrid with DESSs is studied, and the obtained results can provide relevant guidance for system parameter design.

II. System Structure of a DC Microgrid with a DESS

DESS should be configured with a specific capacity to provide energy support and increase system redundancy, thereby ensuring safe and stable operation of the DC microgrid [33]-[35]. Figure 1 shows the system structure of a DC microgrid with a DESS.

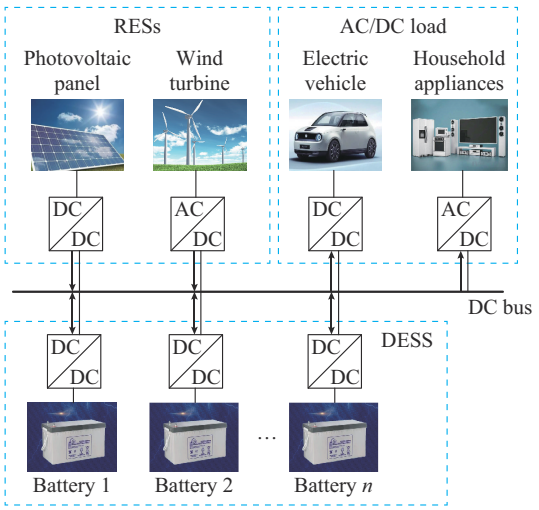

Fig. 1. System structure of a DC microgrid with a DESS.

The system is mainly composed of renewable energy sources (RESs), DESS, loads, various converters, and their control circuits. The photovoltaic panel and wind turbine transmit power to the DC bus through unidirectional DC/DC and AC/DC converters, respectively. Each ESU in the DESS

absorbs or releases power to the DC bus via a bidirectional DC/DC converter. Loads are the main power-consumption components in a DC microgrid, which can directly or indirectly access the DC bus through the converter. When RES produces more power than the load consumption, DESS absorbs the excess power in the form of a charge. When RES produces less power than the load consumption, DESS generates a power deficit in the form of a discharge.

When the DESS operates, the load power of each ESU should be balanced, i.e., should have SOC balance, to avoid the premature exit of some ESUs due to overcharge or overdischarge, which may affect the service life of DESS and the stable operation of DC microgrid [36], [37]. Therefore, designing reasonable control algorithms to realize fast SOC balance in each ESU in a DESS has important theoretical research value and practical engineering significance.

Droop control has the advantages of high reliability and strong flexibility while offering plug-and-play capabilities and easy implementation. It can be used in the control process of ESU energy storage converters [38], [39]. This paper focuses on the droop control strategy of a DESS in a DC microgrid. The corresponding control structure is shown in Fig. 2, where PWM is short for pulse width modulation. Here, the voltage source U_s, including the internal resistance R_s, and switch S are introduced to simulate the power change in the microgrid to simplify the control structure and subsequent research. The circuit changes the charge and discharge modes of the ESUs by switching S on and off.

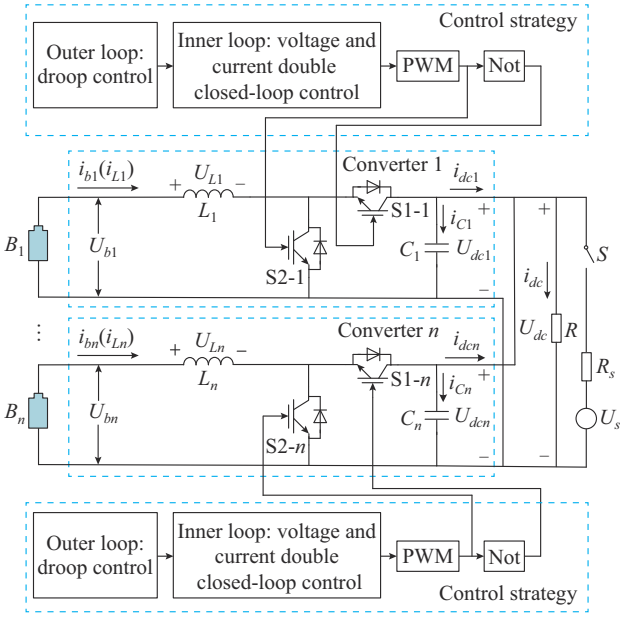

Fig. 2. Control structure of a DC microgrid with a DESS.

In Fig. 2, B_i represents the i^{th} battery; U_{bi} and i_{bi} are the output voltage and output current of the i^{th} battery, respectively; L_i and C_i are the filter inductance and filter capacitance of the energy storage converter for the i^{th} battery, respectively; i_{Li} is the current flowing through L_i; U_{Li} is the terminal voltage of L_i; i_{Ci} is the current flowing through C_i; i_{dc} and U_{dc} are the current and voltage of the DC bus, respectively; R is the load; and U_{dci} and i_{dci} are the actual output voltage and current of the energy storage converter for the i^{th} battery, respectively.

III. Improved Droop Control Strategy

A. I-U Droop Control

DESS in DC microgrid often adopts the *I-U* droop control, which can be expressed as:

$$U_{dci} = U_{refi} - R_{di} i_{dci} \tag{1}$$

where U_{refi} and R_{di} are the reference output voltage and virtual resistance, i.e., droop coefficient, of the i^{th} energy storage converter, respectively.

The operation of two ESUs in parallel is used as an example to illustrate the basic principle of *I-U* droop control. Figure 3 shows the corresponding Thevenin equivalent circuit.

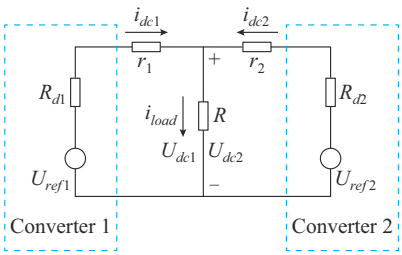

Fig. 3. Corresponding Thevenin equivalent circuit of two ESUs in parallel.

In Fig. 3, r_1 and r_2 are the line impedences of the two ESUs, respectively; and i_{load} is the current flowing through the equivalent load. According to the figure, the corresponding Kirchoff's voltage law (KVL) equation can be expressed as:

$$\begin{cases} U_{dc1} = U_{ref1} - \left(R_{d1} + r_1\right) i_{dc1} \\ U_{dc2} = U_{ref2} - \left(R_{d2} + r_2\right) i_{dc2} \end{cases} \tag{2}$$

Since $U_{dc1} = U_{dc2}$ and the reference voltage of the energy storage converter is usually determined by the DC bus voltage reference value, $U_{ref1} = U_{ref2}$, the relationship between the output currents of two ESUs can be obtained by:

$$\frac{i_{dc1}}{i_{dc2}} = \frac{R_{d2} + r_2}{R_{d1} + r_1} \tag{3}$$

When $R_{d1} < R_{d2}$ and $r_1 < r_2$ are assumed, the droop curve considering the effects of line impedance can be generated, as shown in Fig. 4.

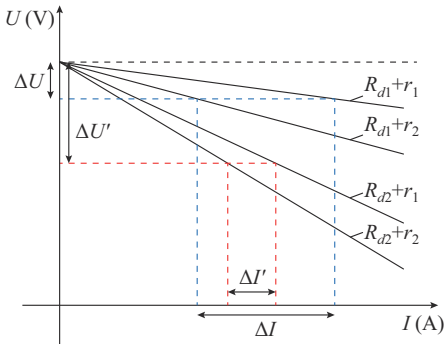

Fig. 4. Droop curve considering effects of line impedance.

In Fig. 4, ΔU and $\Delta U'$ represent variations in voltage, and ΔI and $\Delta I'$ represent deviations of current distribution. As Fig. 4 shows, the greater the virtual resistance, the smaller the effects of line impedance, the higher the distribution accuracy of the current, and the higher the voltage drop, and vice versa. Therefore, when the droop coefficient in the *I-U* droop control is fixed, the DC bus voltage cannot be adequately stabilized.

When the line impedance is significantly less than the virtual impedance, its effect on the line impedance can be ignored. Equation (3) can then be simplified as:

$$\frac{i_{dc1}}{i_{dc2}} \approx \frac{R_{d2}}{R_{d1}} \tag{4}$$

Thus, the relationship between output power P_1 and P_2 of the two ESUs can be obtained as:

$$P_1 R_{d1} = P_2 R_{d2} \tag{5}$$

Equation (5) shows that the output power of ESU is inversely proportional to its droop coefficient. Therefore, when the droop coefficient in the *I-U* droop control is fixed, the output power of each ESU remains unchanged, and the load power cannot be automatically and reasonably allocated according to its own characteristics to achieve SOC balance.

In addition, the voltage drop ΔU_i can be expressed by the virtual resistance as:

$$\Delta U_i = U_{refi} - U_{dci} = R_{di} i_{dci} \tag{6}$$

The voltage drop is proportional to the virtual resistance, and the value range of the virtual resistance can be obtained by:

$$\left| R_{di} \right| \le \frac{\left| \Delta U_{im} \right|}{I_{im}} = \frac{\left| U_{refi} - U_{dci} \right|}{I_{im}} \tag{7}$$

where ΔU_{im} is the maximum allowable voltage deviation; and I_{im} is the full-load current of the i^{th} energy storage converter.

B. SOC Fuzzy Droop Control

The defects in the *I-U* droop control lead to its inability to meet the DESS control requirements, which are mainly reflected in the uneven load power distribution and difficult SOC balance in ESUs. If the relationship between the battery SOC and droop coefficient R_d is established using fuzzy logic, R_d will automatically adjust according to the battery SOC. This dynamic adjustment to the output power of each ESU results in a consistent SOC.

Common methods for estimating battery SOC include the ampere-hour integral method, open-circuit voltage method, internal resistance method, extended Kalman filter method, and neural network method [40], [41]. Among them, the ampere-hour integral method, also known as the Coulomb counting method, is widely used because it is simple and fast operated.

The calculation for estimating the battery SOC using the ampere-hour integral method is:

$$SOC_i(t) = SOC_i(0) - \frac{1}{C_{ei}} \int_0^t i_{bi} \mathrm{d}t \tag{8}$$

where $SOC_i(t)$ and $SOC_i(0)$ are the current and initial SOCs of the i^{th} battery, respectively; C_{ei} is the rated capacity of the i^{th} battery; and i_{bi} is the output current of the i^{th} battery, which is positive when discharged and negative when charged.

We can take the derivative from both ends of (8) to obtain:

$$SOC_i'(t) = -\frac{i_{bi}}{C_{ei}} \tag{9}$$

Equation (9) shows that the rate of change in the battery SOC is directly proportional to the output current. Specifically, during ESU charge, the higher the charge current, the higher the SOC growth rate. During ESU discharge, the higher the discharge current, the higher the SOC decline rate.

It is difficult to quantify the relationship between the battery SOC and R_d. However, it can be effectively expressed through a fuzzy logic relationship. Figure 5 shows the SOC fuzzy droop control scheme, where PI is short for proportional integral.

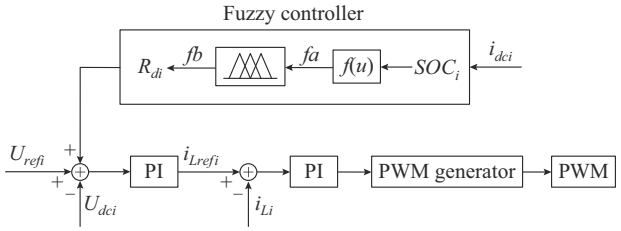

Fig. 5. SOC fuzzy droop control scheme.

In Fig. 5, *fa* and *fb* represent the input and output variables of the fuzzy controller, respectively; and $f(u)$ indicates the functional relationship. The fuzzy controller in this paper adopts the Mamdani type, and its basic structure is shown in Fig. 6.

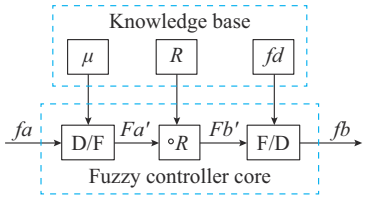

Fig. 6. Basic structure of a fuzzy controller.

In Fig. 6, μ, *R*, and *fd* denote libraries for the membership function, control rule, and defuzzification method, respectively; D/F denotes the fuzzification; *R* is the approximate inference; F/D denotes the defuzzification; and *Fa′* and *Fb′* are the input and output fuzzy quantities, respectively. The design principle of the fuzzy controller is described as follows.

1) Determine Structure of Fuzzy Controller

To ensure that the SOC of each ESU achieves regular consistency, *fa* and *fb* should be selected as the variables associated with the SOC and R_d:

$$\begin{cases} fa = f\left(SOC_i\right) = SOC_i^n - SOC_A^n \\ fb = R_{di} \end{cases} \tag{10}$$

where SOC_A is the average SOC of all ESUs; and super-

script n denotes a constant. Equation (10) shows that the SOC of each ESU eventually tends toward an average SOC_A, and the value of n can be changed to properly adjust the equilibrium speed.

The SOCs of the ESUs during DESS operation are not different. Therefore, the numerical domain of the input variable fa is $[-0.5, 0.5]$. To ensure the effect of drop control, the numerical domain of fb is determined using (7), and the range of fb is $[0, 5]$.

2) Define Fuzzy Distribution of Input and Output Variables

Seven fuzzy subsets {NB, NM, NS, ZO, PS, PM, PB} are selected to cover the fuzzy domain of fa, and all fuzzy subsets are selected as triangular membership functions. NB, NM, NS, ZO, PS, PM, and PB represent negative large, negative medium, negative small, zero, positive small, positive medium, and positive large, respectively. The membership function expression for fa is given by (11). Similarly, seven fuzzy subsets {NB, NM, NS, ZO, PS, PM, PB} are selected to cover the fuzzy domain of fb, and all fuzzy subsets are selected as triangular membership functions. The membership function expression for fb is given by (12). The distributions of the membership functions of fa and fb are shown in Fig. SA1 of Supplementary Material A.

$$\mu_i(fa)=\begin{cases}0 & fa<(i-1)w_{fa}\\ \dfrac{fa-(i-1)w_{fa}}{w_{fa}} & (i-1)w_{fa}\le fa<iw_{fa}\\ -\dfrac{fa-(i+1)w_{fa}}{w_{fa}} & iw_{fa}\le fa<(i+1)w_{fa}\\ 0 & fa\ge(i+1)w_{fa}\end{cases} \tag{11}$$

$$\mu_j(fb)=\begin{cases}0 & fb<(j-1)w_{fb}\\ \dfrac{fb-(j-1)w_{fb}}{w_{fb}} & (j-1)w_{fb}\le fb<jw_{fb}\\ -\dfrac{fb-(j+1)w_{fb}}{w_{fb}} & jw_{fb}\le fb<(j+1)w_{fb}\\ 0 & fb\ge(j+1)w_{fb}\end{cases} \tag{12}$$

where i and j are the numbers of fuzzy subsets of fa and fb, respectively; $\mu_i(fa)$ and $\mu_i(fb)$ are the membership degrees of fa and fb, respectively; and w_{fa} and w_{fb} are the distances between the center points of adjacent membership functions in input and output membership functions, respectively. Fuzzification is the process of identifying the relative fuzzy subsets of fa and their membership functions.

3) Establish Fuzzy Rules

The purpose of establishing fuzzy rules is to select an appropriate R_{di} according to the different inputs fa. For an ESU with a high SOC (where the corresponding input fa is larger), a smaller R_{di} should be allocated during discharge to increase the discharge power, and a larger R_{di} should be allocated during charge to reduce the charge power. For an ESU with a low SOC (where the corresponding input fa is small), a larger R_{di} should be allocated during discharge to reduce the discharge power, and a smaller R_{di} should be allocated during charge to increase the charge power. The SOC balance in ESUs can be realized by meeting these requirements.

The change from NB to PB in the fuzzy subset corresponds to a change in the language variables from small to large. Therefore, linguistic fuzzy rules can be obtained. For example, when ESU is discharged, fa is PB (large) and R_{di} is NB (small), and so on. The fuzzy rules are obtained by sorting the obtained linguistic fuzzy rules, as shown in Table I, where Fa and Fb are fuzzy input and output variables, respectively.

TABLE I
FUZZY RULES

ESU charge ($i_{dc}<0$)		ESU discharge ($i_{dc}>0$)	
Fa	Fb	Fa	Fb
NB	NB	NB	PB
NM	NM	NM	PM
NS	NS	NS	PS
ZO	ZO	ZO	ZO
PS	PS	PS	NS
PM	PM	PM	NM
PB	PB	PB	NB

4) Approximate Inference

The process of reasoning in a signed syllogism is as follows: ① major premise: $Fa(fa)\rightarrow Fb(fb)$; ② minor premise: $Fa'(fa)$; and ③ conclusion: $Fb'(fb)$.

The i^{th} fuzzy relation R_i determined by the i^{th} fuzzy rule $F_{ai}\rightarrow F_{bi}$ is given by (13). When the control rule base contains n fuzzy rules, the total fuzzy relationship is expressed by (14).

$$R_i(fa,fb)=\mu_{F_{a_i}\times F_{b_i}}(fa,fb)=\mu_{F_{a_i}}(fa)\bigwedge\mu_{F_{b_i}}(fb) \tag{13}$$

$$R=\bigcup_{i=1}^{n}R_i \tag{14}$$

where μ is the membership degree.

The fuzzy set Fb' in the conclusion is determined by using the minor premise Fa', as shown in (15), and the corresponding fuzzy membership function is given by (16).

$$Fb'=Fa'\circ R=Fa'\circ\bigcup_{i=1}^{n}R_i \tag{15}$$

$$\mu_{Fb'}(fb)=\bigvee_{i=1}^{m}\left[\mu_{Fa'}(fa)\bigwedge\left(\bigvee_{i=1}^{n}\mu_{F_{a_i}\times F_{b_i}}(fa,fb)\right)\right] \tag{16}$$

where $\circ$ represents the compositional operation; and m is the number of active rules.

5) Defuzzification

The output obtained by the approximate inference is a fuzzy set Fb', which must be converted into an exact numerical quantity fb to control the controlled object, i.e., defuzzification. When the area-center method is used for defuzzification, fb is expressed as:

$$fb=\frac{\int \mu_{Fb}(fb)\cdot fb\mathrm{d}(fb)}{\int \mu_{Fb}(fb)\mathrm{d}(fb)} \tag{17}$$

Following this process, a one-dimensional fuzzy relationship between *fa* and *fb* is obtained. The relationship between *fa* and *fb* during the charge and discharge of the ESU is shown in Fig. SA2 of Supplementary Material A.

C. Design of Acceleration Factor

Under the gradual SOC balance process, the SOC difference among ESUs becomes increasingly smaller. The fuzzy input *fa* of each ESU tends to be the same. Therefore, the fuzzy output *fb*, i.e., R_{di}, also tends to be the same. According to (4) and (5), the output current and power of each ESU change slowly, which are not conducive to load power distribution and greatly reduce the speed and accuracy of the SOC balance.

To solve this problems, an acceleration factor is added to the late stage of the SOC balance. The value of the fuzzy input *fa* is dynamically changed mainly by multiplying it with other functions to improve the resolution between the SOC and R_d of each ESU. The designed acceleration factor K is expressed as:

$$K=\frac{m_1}{\exp\left(m_2\left|fa\right|\right)}=\frac{m_1}{\exp\left(m_2\left|SOC_i^n-SOC_A^n\right|\right)} \tag{18}$$

where m_1 and m_2 are the constants.

Equation (18) shows that K is related to m_1 and m_2, and $fa=SOC_i^n-SOC_A^n$. Figure 7 shows the relationships among the different variables.

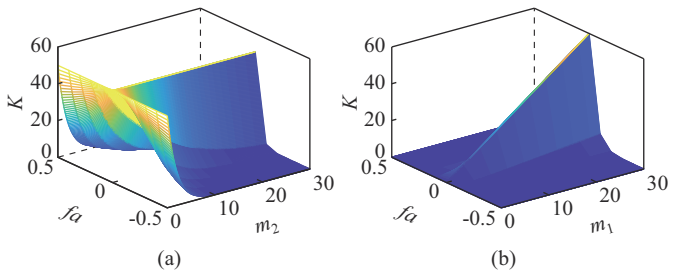

Fig. 7. Relationships among different variables. (a) K, m_2, and *fa*. (b) K, m_1, and *fa*.

Figure 7(a) shows that when m_1 is fixed, K gradually decreases with an increase in m_2, and K first increases and then decreases with an increase in *fa*, reaching the maximum when *fa* is zero. Figure 7(b) shows that when m_2 is fixed, K gradually increases with an increase in m_1, and the variation trend of K with *fa* is consistent with that shown in Fig. 7(a). In the balance process, the SOC of each ESU gradually tends toward SOC_A. In other words, $\left|SOC_i^n-SOC_A^n\right|$ slowly approaches zero; thus, K gradually increases to m_1.

The change process of K from small to large not only can avoid the excessive output current of some ESUs caused by the large difference in the droop coefficient in the early stage of equalization, but also can ensure the resolution of the droop coefficient in the late stage of equalization to improve the SOC balance speed and accuracy. The modified fuzzy input fa^m can be expressed as:

$$fa^m=K\cdot fa=\frac{m_1\left(SOC_i^n-SOC_A^n\right)}{\exp\left(m_2\left|SOC_i^n-SOC_A^n\right|\right)} \tag{19}$$

IV. Stability Analysis of Microgrid

A. Average Model of ESU

The converters in the DESS are bidirectional DC/DC converters, and their specific circuit structures are shown in Fig. 2. The average model of the i^{th} bidirectional DC/DC converter can be expressed as:

$$\begin{cases}U_{Li}=U_{bi}-D_{1i}U_{dci}\\ i_{Ci}=D_{1i}i_{Li}-i_{dci}\end{cases} \tag{20}$$

where D_{1i} is the average duty cycle of the upper bridge arm switch tube S_{1i}; and U_{bi} is the equivalent voltage of the i^{th} ESU.

The calculation for the inductance voltage and capacitance current in circuit theory is:

$$\begin{cases}U_{Li}=L_i\dfrac{\mathrm{d}i_{Li}}{\mathrm{d}t}\\ i_{Ci}=C_i\dfrac{\mathrm{d}U_{Ci}}{\mathrm{d}t}\end{cases} \tag{21}$$

where U_{Ci} is the terminal voltage of C_i.

Equation (21) can be substituted into (20), and an inverse Laplace transform can be applied to obtain the average model expression of the bidirectional DC/DC converter in the frequency domain.

$$\begin{cases}i_{Li}=\left(U_{bi}-D_{1i}U_{dci}\right)/\left(L_is\right)\\ U_{Ci}=\left(D_{1i}i_{Li}-i_{dci}\right)/\left(C_is\right)\end{cases} \tag{22}$$

A structural block diagram of the bidirectional DC/DC converter derived from (22) is presented as Fig. 8.

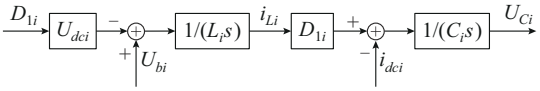

Fig. 8. Structural block diagram of a bidirectional DC/DC converter.

The control of the bidirectional DC/DC converter has a double-loop control structure, in which the outer and inner loops adopt droop and voltage-current double closed-loop PI controls, respectively. A control block diagram of the bidirectional DC/DC converter is given in Fig. 9.

In Fig. 9, D_{2i} is the average duty cycle of the lower bridge arm switch tube S_{2i}, $D_{2i}=1-D_{1i}$; and $G_{ui}(s)$ and $G_{ii}(s)$ are the transfer functions of the voltage and current controllers, respectively, which are expressed as:

$$\begin{cases}G_{ui}(s)=k_{up,i}+\dfrac{k_{ui,i}}{s}\\ G_{ii}(s)=k_{ip,i}+\dfrac{k_{ii,i}}{s}\end{cases} \tag{23}$$

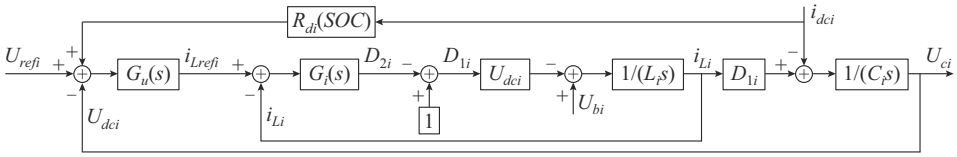

Fig. 9. Control block diagram of a bidirectional DC/DC converter.

where $k_{up,i}$ and $k_{ui,i}$ are the proportional and integral coefficients of the voltage controller, respectively; and $k_{ip,i}$ and $k_{ii,i}$ are the proportional and integral coefficients of the current controller, respectively.

Figure 9 shows the closed-loop output impedance of the i^{th} ESU in the frequency domain as:

$$\begin{cases} Z_i = \dfrac{U_{dci}}{i_{dci}} = Z_{i1} = Z_{i2} \\ Z_{i1} = \dfrac{\left(R_{di}(SOC)G_{ui}(s)G_{Ai}(s)D_{1i}-1\right)/\left(C_i s\right)}{1+G_{ui}(s)G_{Ai}(s)D_{1i}/\left(C_i s\right)} \quad i_{dci}>0 \\ Z_{i2} = -Z_{i1} \quad i_{dci}<0 \end{cases} \tag{24}$$

where Z_{i1} is the equivalent output impedance during discharge; Z_{i2} is the equivalent output impedance during charge; and $G_{Ai}(s)$ is the equivalent transfer function in the simplification process, which is expressed as:

$$G_{Ai}(s) = \frac{G_{ii}(s)U_{dci}/\left(L_i s\right)}{1+G_{ii}(s)U_{dci}/\left(L_i s\right)} \tag{25}$$

In addition, the closed-loop transfer function of the i^{th} ESU $G_{oi}(s)$ can be obtained as:

$$G_{oi}(s) = \frac{U_{dci}(s)}{U_{refi}(s)} + \frac{U_{dci}(s)}{i_{dci}(s)} = \frac{G_{ui}(s)G_{Ai}(s)D_{1i}/\left(C_i s\right)}{1+G_{ui}(s)G_{Ai}(s)D_{1i}/\left(C_i s\right)} + \frac{\left(R_{di}(SOC)G_{ui}(s)G_{Ai}(s)D_{1i}-1\right)/\left(C_i s\right)}{1+G_{ui}(s)G_{Ai}(s)D_{1i}/\left(C_i s\right)} \tag{26}$$

The impedance characteristics and the ESU stability can be analyzed using (24) and (26), respectively.

B. Stability Criteria of Microgrid

Impedance ratio analysis is commonly used to study the stability of a microgrid. The steps are as follows. First, the microgrid is divided into multiple submodules, each of which can be regarded as a two-terminal network. Then, each two-terminal network undergoes an equivalent treatment based on the Thevenin theorem. The two-terminal network is represented by the series form of the voltage source and resistance. Finally, the impedance ratio of the system is calculated using the circuit equivalent principle, and the stability of the microgrid is determined based on the Nyquist curve of the impedance ratio. The DC microgrid with a DESS as shown in Fig. 2 is equivalent to the circuit form shown in Fig. 10. In Fig. 10, Z_r is the equivalent impedance of the load.

The microgrid is often equivalent to the power supply and load subsystems. This equivalence enables system stability to be analyzed under the disturbance of each frequency band. When switch S is turned off, each ESU is in the charge mode, which is regarded as a load and integrated into the load subsystem. When switch S is turned on, each ESU is in the discharge mode, which is regarded as a micropower supply and is integrated into the power supply subsystem. This process is illustrated in Figs. 11 and 12.

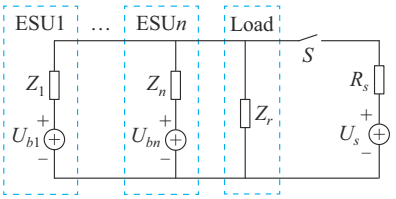

Fig. 10. Thevenin equivalent circuit of a DC microgrid with a DESS.

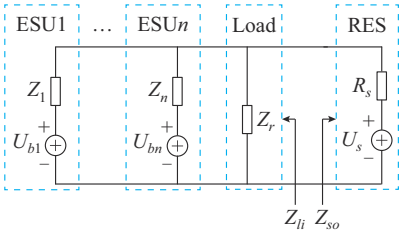

(a)

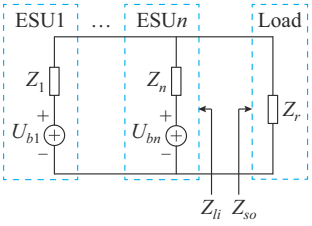

(b)

Fig. 11. Equivalent circuit of a microgrid during ESU charge or discharge. (a) ESU charge. (b) ESU discharge.

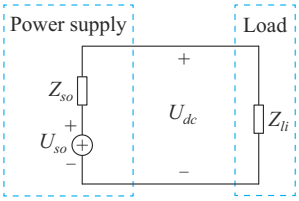

Fig. 12. Unified circuit model of a microgrid.

In Fig. 11, Z_{so} and Z_{li} are the equivalent output impedances of the power supply and load subsystems, respectively. The calculations for Z_{so} and Z_{li} during DESS charge and discharge are given by (27) and (28), respectively.

$$\begin{cases} Z_{so} = R_s \\ \dfrac{1}{Z_{li}} = \dfrac{1}{Z_1} + \dfrac{1}{Z_2} + \cdots + \dfrac{1}{Z_n} + \dfrac{1}{Z_r} = \displaystyle\sum_{i=1}^{n}\frac{1}{Z_i} + \frac{1}{Z_r} \end{cases} \tag{27}$$

$$\begin{cases} \dfrac{1}{Z_{so}} = \dfrac{1}{Z_1} + \dfrac{1}{Z_2} + \cdots + \dfrac{1}{Z_n} = \sum_{i=1}^{n} \dfrac{1}{Z_i} \\ Z_{li} = Z_r \end{cases} \tag{28}$$

In Fig. 12, U_{so} is the output voltage of the power supply subsystem. When U_{so} is accompanied by disturbance $\hat{u}_{so}$, U_{dc} generates disturbance $\hat{u}_{dc}$, and their relationship can be expressed as:

$$\frac{\hat{u}_{dc}}{\hat{u}_{so}} = \frac{1}{1 + Z_{so}/Z_{li}} \tag{29}$$

Equation (29) shows that the DC bus voltage is directly related to the system impedance ratio Z_{so}/Z_{li}. Simultaneously, the stability criterion of the microgrid can be obtained under the following condition: when the Nyquist curve of Z_{so}/Z_{li} does not contain point $(-1, 0)$, the microgrid is in stable operation.

V. Simulation Validation

A. Parameter Settings

Droop control methods based on the SOC exponential and SOC power functions are proposed in [16] and [17], respectively. The specific expressions for droop control in these two methods are respectively given as:

$$R_{di}(SOC_i) = \begin{cases} R_D \exp\left(p\left(SOC_i - SOC_A\right)\right) & i_{dc} < 0 \\ R_D \exp\left(-p\left(SOC_i - SOC_A\right)\right) & i_{dc} > 0 \end{cases} \tag{30}$$

$$R_{di}(SOC_i) = \begin{cases} R_D \cdot SOC_i^n & i_{dc} < 0 \\ R_D / SOC_i^n & i_{dc} > 0 \end{cases} \tag{31}$$

where R_D is the droop coefficient of the energy storage converter at full-load current; and p is a constant. The ESU is charged when $i_{dc} < 0$ and is discharged when $i_{dc} > 0$.

These two methods are compared with the proposed method. With two ESUs used as examples to conduct the simulation research, the specific parameter settings are listed in Table II.

TABLE II
Parameter Settings

Parameter	Value
Reference value of DC bus voltage	400 V
Bus voltage fluctuation range	±5%
ESU1: L_1, C_1, $k_{up,1}(k_{ui,1})$, $k_{ip,1}(k_{ii,1})$, SOC_1	0.3 mH, 300 μF, 2(20), 3(3), 60%
ESU2: L_2, C_2, $k_{up,2}(k_{ui,2})$, $k_{ip,2}(k_{ii,2})$, SOC_2	0.3 mH, 300 μF, 2(20), 3(3), 58%
m_1, m_2, n	50, 20, 3
Load	8 kW

B. Stable Charge and Discharge

When the output power of RES exceeds the load demand, the DESS is in a stable charge mode. This situation can be simulated by closing switch S, as shown in Fig. 2. Figure 13 shows the DESS state (SOC and output power P) during steady charge. Notably, j-ESU$_i$ ($i = 1, 2$, $j = 1, 2, 3$) in the figure is the i^{th} ESU of the j^{th} droop control method, $j = 1$ is the SOC exponential function droop control in [16], $j = 2$ is the SOC power function droop control in [17], and $j = 3$ is the method proposed in this paper. In addition, SOC differences and power differences are defined to reflect control performances when $\Delta SOC = SOC_{ESU1} - SOC_{ESU2}$ and $\Delta P = P_{ESU1} - P_{ESU2}$.

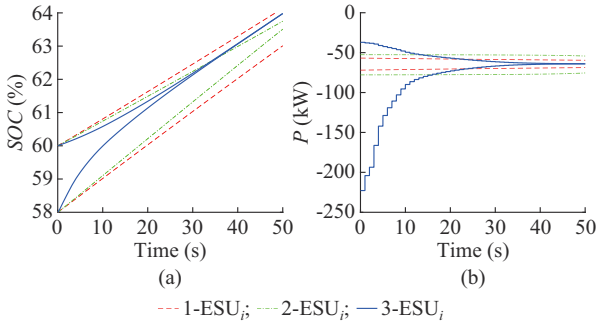

Fig. 13. DESS state during steady charge. (a) SOC. (b) Output power.

Figure 13 shows that during the period [0, 50]s, when the SOC exponential function drop control is adopted, ΔSOC and ΔP between ESUs decrease from 2% to 1.1% and from 15.1 kW to 9.2 kW, respectively. When the SOC power function droop control is adopted, ΔSOC and ΔP between ESUs decrease from 2% to 0.2% and from 25.3 kW to 21.2 kW, respectively. When the SOC fuzzy droop control is adopted, ΔSOC and ΔP between ESUs decrease from 2% to 0 and from 196.2 kW to 0 kW at 41.5 s, respectively. These results show that in terms of the rapidness and accuracy of the SOC balance and load power distribution, the best performance is achieved by the SOC fuzzy droop control, followed by the SOC power function and SOC exponential function droop controls.

The DESS state during steady discharge under different droop control methods is shown in Fig. SA3 of Supplementary Material A.

C. Changes of Charge and Discharge Modes

When the power of the supply and demand sides of the DC microgrid is not equal, the charge and discharge modes of the DESS change. The supply- and demand-side power refers to the output power of the RES and power consumed by the loads, respectively. In this paper, the simulation duration is 60 s, and the state of switch S is changed from closed to open at 30 s to simulate a power change situation. Figure 14 shows the DESS state when charge and discharge modes change.

As Fig. 14 shows, the balance time of the SOC exponential function droop control exceeds 60 s, whereas those of the SOC power function and SOC fuzzy droop controls are 55.2 s and 48.6 s, respectively. The superiority of the SOC fuzzy droop control in terms of the SOC balance and load distribution is further explained. The SOC fuzzy droop control requires the shortest time to complete the balance, indicating that this method still performs better when the DESS

charge and discharge modes change. In addition, the DESS state under a sudden change in load is shown in Fig. SA4 of Supplementary Material A.

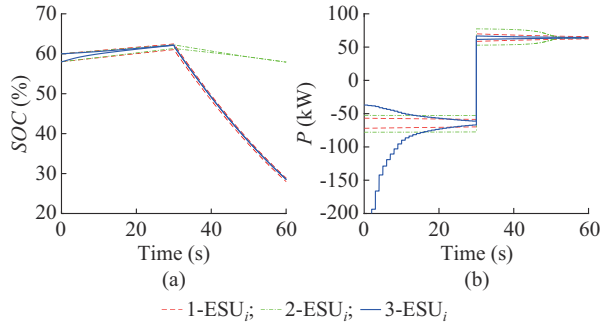

Fig. 14. DESS state when charge and discharge modes change. (a) SOC. (b) Output power.

D. Effect of Acceleration Factor

The acceleration factor is introduced to improve the resolution of the SOC differences among the ESUs. This enables a fast equalization speed to be maintained in the later stages. The duration of the simulation is 40 s, and the state of switch S is changed from closed to open at 20 s. Accordingly, the SOC fuzzy drop control method is simulated with and without the acceleration factor. Figure 15 shows the corresponding changes in the DESS state, where a-ESU$_i$ and b-ESU$_i$ denote ESUs without and with an acceleration factor, respectively.

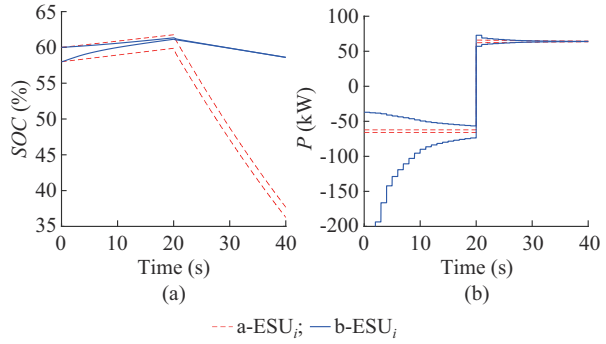

Fig. 15. DESS state with and without an acceleration factor. (a) SOC. (b) Output power.

As Fig. 15 shows, the balance time of the SOC fuzzy droop control without an acceleration factor exceeds 40 s, whereas that with an acceleration factor is 35.2 s. The SOC fuzzy droop control with an acceleration factor is clearly better than that without an acceleration factor with respect to SOC balance speed, which shows that the design of the acceleration factor is reasonable and effective.

The design method for the acceleration factor is not unique and mainly consists of an exponential function, logarithmic function, power function, and other basic functions. The exponential and logarithmic functions are suitable for describing the change laws of fast and slow growth rates, respectively, and the power function resides between the two and is thus suitable for describing the change law of the general growth rate. Therefore, several types of the acceleration factors are designed as:

$$\begin{cases} K_1 = \dfrac{m_1}{\ln\left(m_2 \left| fa \right|\right)} \\ K_2 = \dfrac{m_1}{\left(m_2 \left| fa \right|\right)^{\mathrm{e}}} \\ K_3 = \dfrac{m_1}{\exp\left(m_2 \left| fa \right|\right)} = K \end{cases} \tag{32}$$

Different types of acceleration factors have different effects on the SOC balance speed and power distribution accuracy. Under the condition in which the charge and discharge modes of the DESS change, i. e., where the charge mode changes to the discharge mode at 30 s, the SOC fuzzy drop control under different types of acceleration factors is simulated. The DESS state under different acceleration factors is shown in Fig. 16.

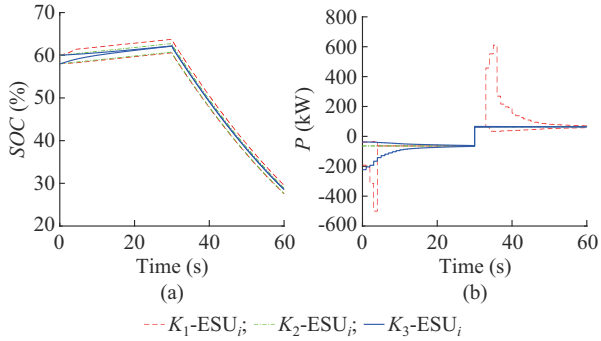

Fig. 16. DESS state with different acceleration factors. (a) SOC. (b) Output power.

As Fig. 16(a) shows, when the SOC fuzzy droop control with acceleration factors K_1, K_2, and K_3 is adopted, the ΔSOC between ESUs changes from 2% to 3.16%, 1.95%, and 0.05% during the period [0, 30]s, and it continues to change to 1.98%, 1.25%, and 0 during the period [30, 60]s. The SOC fuzzy drop control with K_3 reaches an SOC balance at 42.4 s, whereas the that with K_1 and K_2 has a balance time of more than 60 s, indicating that the performance of the SOC fuzzy droop control with K_3 is optimal. Notably, the SOC fuzzy drop control with K_1 increases the ΔSOC between ESUs during the period [0, 4.2]s, which is mainly caused by the change rate characteristics of the logarithmic function.

As Fig. 16(b) shows, the power distribution imbalance of the SOC fuzzy droop control with K_1 during the periods [1, 4]s and [33, 36]s, i. e., ESU discharges and charges with lower and higher SOCs, respectively, causes the equilibrium rate to slow down, while that with K_2 shows little change in ΔP between ESUs during the period [0, 60]s. A longer period is required to achieve SOC balance. ΔP of SOC fuzzy droop control with K_3 shows a higher resolution during the period [0, 60]s and therefore achieves a better balance rate and accuracy during the entire period.

E. Comparative Analysis of Performance Index

To obtain an accurate evaluation of how well the fuzzy controller performs with the added exponential acceleration factor and to assess the performances of the other controllers, the performance index J is introduced, as shown in (33), where J reflects the SOC balance accuracy of multiple ESUs at a specific time during the DESS balance process. A smaller J indicates better controller performance, and faster SOC balance can then be achieved.

$$J(t)=\frac{SOC_i(t)-SOC_j(t)}{SOC_i(0)-SOC_j(0)} \tag{33}$$

where $SOC_j(t)$ and $SOC_j(0)$ are the current and initial SOCs of the j^{th} ESU, respectively.

Table III lists J under different control methods. In Table III, M1, M2, and M3 represent the i^{th} droop control method for SOC exponential function droop, SOC power function droop, and SOC fuzzy droop, respectively. In addition, K_0 is the SOC fuzzy drop with no acceleration factor. Finally, M3 and M3-K_3 are the methods proposed in this paper. The simulation conditions for Situations 3 and 4 are set as the same; that is, DESS changes from the charge mode to discharge mode at 30 s.

TABLE III
J UNDER DIFFERENT CONTROL METHODS

Situation	Method	J				
		t=10 s	t=20 s	t=30 s	t=40 s	t=50 s
1. Stable charge	M1	0.895	0.800	0.715	0.635	0.565
	M2	0.820	0.640	0.460	0.285	0.120
	M3	0.295	0.100	0.025	0.005	0
2. Stable discharge	M1	0.875	0.745	0.620	0.500	0.390
	M2	0.720	0.450	0.200	0.015	0
	M3	0.250	0.055	0.010	0	0
3. Change of charge and discharge modes	M1	0.895	0.800	0.715	0.630	0.540
	M2	0.820	0.640	0.460	0.205	0.015
	M3	0.295	0.100	0.025	0.020	0
4. Effects of acceleration factor	M3-K_0	1.000	0.995	0.990	0.880	0.755
	M3-K_1	1.580	1.585	1.580	1.390	1.195
	M3-K_2	0.970	0.945	0.915	0.805	0.690
	M3-K_3	0.295	0.100	0.025	0.020	0

As Table III shows, J with method M3-K_1 under Situation 4 shows a trend of first increasing and then decreasing with time, whereas those with the other methods under various working conditions gradually decrease with time. This shows that method M3-K_1 reduces the SOC balance speed between ESUs but eventually achieves SOC balance. It also shows that all methods can achieve the control goal of SOC balance. Moreover, under the same operation conditions, J with methods M1, M2, and M3 decreases successively at specific time, indicating that method M3 performs better than methods M1 and M2. Under Situation 4, taking J with method M3-K_0 as the benchmark, J values of M3-K_1, M3-K_2, and M3-K_3 are greater than, less than, and far less than those of M3-K_0, respectively. This shows that the design of the acceleration factor is reasonable and that the proposed method can significantly improve the SOC balance speed.

F. Run More than Two ESUs

The DESS is set to contain three ESUs with initial SOCs for the three ESUs of 60%, 58%, and 56%, respectively. The DESS changes from the charge mode to discharge mode at 30 s. Figure 17 shows the DESS state under the aforementioned conditions.

As Fig. 17 shows, during the period [0, 60]s and when the SOC exponential function droop control is adopted, ΔSOC between ESU1 and ESU2 and that between ESU2 and ESU3 decrease from 2% to 1.04% and 1.05%, respectively, and ΔP between ESU1 and ESU2 and that between ESU2 and ESU3 decrease from 13.45 kW and 16.39 kW to 7.28 kW and 8.34 kW, respectively. When the SOC power function droop control is adopted, ΔSOC between ESU1 and ESU2 and that between ESU2 and ESU3 decrease from 2% to 0.91% and 0.93%, respectively, and ΔP between ESU1 and ESU2 and that between ESU2 and ESU3 decrease from 11.57 kW and 14.11 kW to 12.52 kW and 12.69 kW, respectively. When the SOC fuzzy droop control is adopted, ESU2 and ESU3 reach a balance at 21.5 s, whereas ESU1, ESU2, and ESU3 reach a balance at 48.4 s. Compared with the SOC exponential and SOC power function droop controls, the SOC fuzzy droop control still has the highest balance speed when the number of ESUs increases, which further reflects the advantages of the proposed method.

G. Stability Analysis 1: ESU

Equation (24) shows that the closed-loop output impedance of the ESU is related to the droop coefficient, voltage PI controller parameters, current PI controller parameters, filter capacitance, and filter inductance. This paper focuses on the effects of the droop coefficient on the closed-loop output impedance of the ESU, and the corresponding Bode diagram is shown in Fig. 18.

As Fig. 18 shows, when the frequency is less than 50 rad/s, the closed-loop output impedance of the ESU increases with the droop coefficient, i.e., the proposed method can improve the power response capability of the ESU in the low-frequency band. When the frequency is in the range of 50-10^8 rad/s, the droop coefficient has little influence on the closed-loop output impedance of the ESU. When the frequency exceeds 10^8 rad/s, the droop coefficient has an insignificant influence on the closed-loop output impedance of the ESU.

Equation (19) shows that an increase in acceleration factor K leads to the increase of fa^m, which resolves $fb=R_{di}$. The numerical domain of fb is determined by the range of R_{di}, as shown in (7). The output of the fuzzy controller is bounded [37], [38]. Therefore, the effects of the acceleration factor on the system stability can be explained by showing that the system stability is within the range of the droop coefficient. The effects of the droop coefficient on the ESU stability is shown in Fig. 19 via (26).

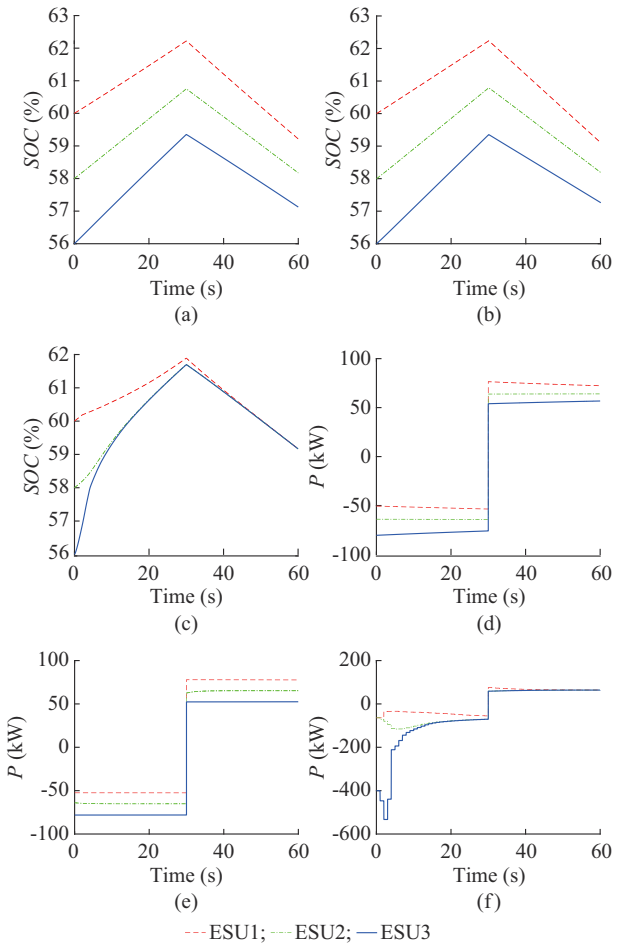

Fig. 17. DESS state with three ESUs. (a) SOC of M1. (b) SOC of M2. (c) SOC of M3. (d) Output power of M1. (e) Output power of M2. (f) Output power of M3.

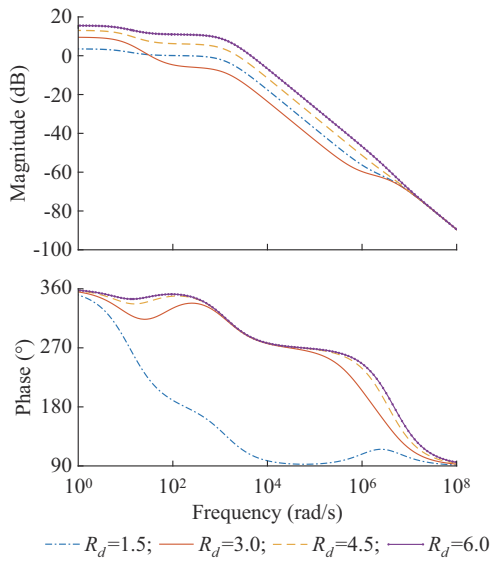

Fig. 18. Effects of droop coefficient on closed-loop output impedance of ESU.

As Fig. 19 shows, when the frequency is less than 2×10^7 rad/s, the amplitude margin of the closed-loop transfer function of ESU increases with the droop coefficient. When the frequency is greater than 2×10^7 rad/s, the variation in droop coefficient has little effect. In addition, with a change in the droop coefficient, the phase angle margin of the closed-loop transfer function of ESU is always positive, indicating that the ESU is stable when the droop coefficient changes within the range expressed in (7). Therefore, the ESU is always stable under the action of an acceleration factor.

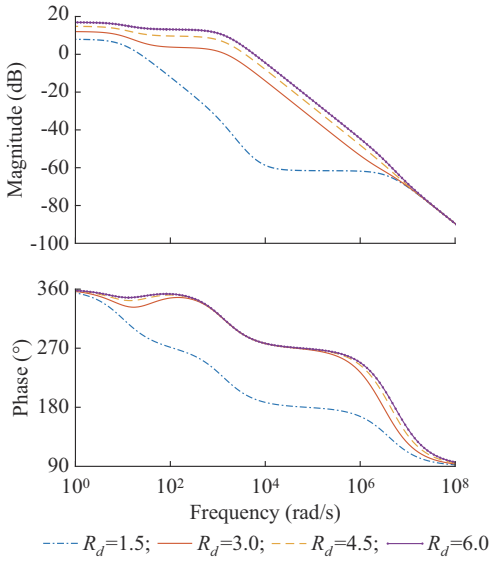

Fig. 19. Effects of droop coefficient on ESU stability.

Because the bandwidth of the voltage PI controller is much smaller than that of the current PI controller, the effects of the voltage PI controller parameters on ESU stability are more obvious. The corresponding Bode diagram is given as Fig. SA5 in Supplementary Material A.

H. Stability Analysis 2: DC Microgrid

The DC microgrid with DESS in this paper has two working modes. ① Mode 1: when the output power of the RES is greater than the load power, the DESS is in the charge mode. ② Mode 2: when the output power of the RES is less than the load power, the DESS is in the discharge mode. If the DC microgrid is stable under both working modes, the overall system is stable.

A DC microgrid with two ESUs is next taken as an example. The equivalent output impedances of the power and load sides of the microgrid in Modes 1 and 2 are given by (34) and (35), respectively.

$$\begin{cases} Z_{so}=R_S \\ Z_{li}=\dfrac{Z_1Z_2Z_r}{Z_1Z_2+Z_1Z_r+Z_2Z_r} \end{cases} \tag{34}$$

$$\begin{cases} Z_{so}=\dfrac{Z_1Z_2}{Z_1+Z_2} \\ Z_{li}=Z_r \end{cases} \tag{35}$$

Equations (34) and (35) show that Z_{so}/Z_{li} of the microgrid in Modes 1 and 2 can be obtained, respectively. Figure 20 shows the Nyquist curves of system impedance ratio of microgrid in Modes 1 and 2.

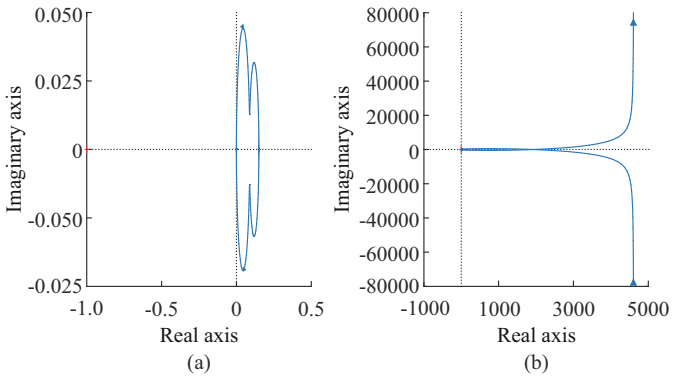

Fig. 20. Nyquist curves of system impedance ratio of microgrid. (a) Mode 1. (b) Mode 2.

As Fig. 20 shows, the Nyquist curves do not include the point $(-1, 0)$, indicating that the microgrid is stable in Modes 1 and 2 and thus verifying the stability of the microgrid system.

In addition, the smaller amplitude and phase angle margins in Modes 1 and 2 are at the lower limits, ensuring the stable operation of the microgrid ($G_{\min} = 12.9$ dB, $P_{\min} = inf$ at 0.0372 rad/s). Thus, the conditions of the system input and output impedances for ensuring the stable operation of the microgrid can be obtained when $|Z_{Li}| > |Z_{so}| + G_{\min}$ and the phase angle of Z_{Li} is not subject to any constraints. When the aforementioned conclusions are applied, it is necessary to obtain the amplitudes and phase angles of the input and output impedances of the system , as shown in (27) and (28). Then, a calculation must be performed to determine whether the condition $|Z_{Li}| > |Z_{so}| + G_{\min}$ is satisfied. If the condition is satisfied, the designed microgrid is stable; otherwise, the parameters of the microgrid must be redesigned.

VI. Conclusion

Autonomous DC microgrids usually contain multiple ESUs for maintaining bus voltage stability and power balance. Therefore, reasonable power distribution and fast SOC balance in ESUs are critical. An SOC fuzzy droop control with an acceleration factor is proposed, and the system stability is investigated based on the average model of the converter.

The following conclusions are obtained. ① The SOC fuzzy droop control has a faster balance speed and accuracy as compared with the SOC exponential and SOC power function droop control. ② The design of the acceleration factor can resolve the SOC between ESUs in the entire equalization process, particularly in the later stages, and this can in turn improve the balance speed. ③ The transfer function of the ESU in the droop control mode is derived, and this paper shows that the ESU continues to operate in a stable manner when the droop coefficient changes. ④ A stability criterion for the DC microgrid with DESS is given, which can provide a reference for parameter design.

In future research, we will address the following challenges. ① The main variables affecting the variation in droop coefficient will be analyzed, and a multidimensional fuzzy logic relationship will be constructed. ② The effects of different fuzzy membership functions and their distributions on the SOC balance performance will be studied to obtain a better fuzzy controller. ③ The form of the acceleration factor is not unique, where a combined acceleration factor is developed to achieve autonomous control of the balance speed. ④ Various modeling theories are used to analyze the stability of the microgrid, and a reasonable application range of the corresponding criteria is provided.

References

[1] H. Hajebrahimi, S. M. Kaviri, S. Eren *et al*., "A new energy management control method for energy storage systems in microgrids," *IEEE Transactions on Power Electronics*, vol. 35, no. 11, pp. 11612-11624, Nov. 2020.

[2] U. Datta, A. Kalam, and J. Shi, "Battery energy storage system control for mitigating PV penetration impact on primary frequency control and state-of-charge recovery," *IEEE Transactions on Sustainable Energy*, vol. 11, no. 2, pp. 746-757, Apr. 2020.

[3] A. Bharatee, P. K. Ray, and A. Ghosh, "A power management scheme for grid-connected PV integrated with hybrid energy storage system," *Journal of Modern Power Systems and Clean Energy*, vol. 10, no. 4, pp. 954-963, Jul. 2022.

[4] M. Berger, I. Kocar, E. Farantatos *et al*., "Dual control strategy for grid-tied battery energy storage systems to comply with emerging grid codes and fault ride through requirements," *Journal of Modern Power Systems and Clean Energy*, vol. 10, no. 4, pp. 977-988, Jul. 2022.

[5] L. Xu, J. M. Guerrero, A. Lashab *et al*., "A review of DC shipboard microgrids – Part II: control architectures, stability analysis, and protection schemes," *IEEE Transactions on Power Electronics*, vol. 37, no. 4, pp. 4105-4120, Apr. 2022.

[6] S. Liu, X. Li, M. Xia *et al*., "Takagi-sugeno multimodeling-based large signal stability analysis of DC microgrid clusters," *IEEE Transactions on Power Electronics*, vol. 36, no. 11, pp. 12670-12684, Nov. 2021.

[7] X. Yang, C. Xu, Y. Zhang *et al*., "Real-time coordinated scheduling for ADNs with soft open points and charging stations," *IEEE Transactions on Power Systems*, vol. 36, no. 6, pp. 5486-5499, Apr. 2021.

[8] Q. Yang, J. Zhou, X. Chen *et al*., "Distributed MPC-based secondary control for energy storage systems in a DC microgrid," *IEEE Transactions on Power Systems*, vol. 36, no. 6, pp. 5633-5644, Nov. 2021.

[9] W. Yan, X. Wang, W. Gao *et al*., "Electro-mechanical modeling of wind turbine and energy storage systems with enhanced inertial response," *Journal of Modern Power Systems and Clean Energy*, vol. 8, no. 5, pp. 820-830, Sept. 2020.

[10] N. Zhi, K. Ding, L. Du *et al*., "An SOC-based virtual DC machine control for distributed storage systems in DC microgrids," *IEEE Transactions on Energy Conversion*, vol. 35, no. 3, pp. 1411-1420, Sept. 2020.

[11] M. Dong, L. Li, Y. Nie *et al*., "Stability analysis of a novel distributed secondary control considering communication delay in DC microgrids," *IEEE Transactions on Smart Grid*, vol. 10, no. 6, pp. 6690-6700, Nov. 2019.

[12] R. Bhosale, R. Gupta, and V. Agarwal, "A novel control strategy to achieve SOC balancing for batteries in a DC microgrid without droop control," *IEEE Transactions on Industry Applications*, vol. 57, no. 4, pp. 4196-4206, Jul. 2021.

[13] K. Bi, L. Sun, Q. An *et al*., "Active SOC balancing control strategy for modular multilevel super capacitor energy storage system," *IEEE Transactions on Power Electronics*, vol. 34, no. 5, pp. 4918-4992, May 2019.

[14] Q. Wu, R. Guan, X. Sun *et al*., "SoC balancing strategy for multiple energy storage units with different capacities in islanded microgrids based on droop control," *IEEE Journal of Emerging and Selected Topic in Power Electronics*, vol. 6, no. 4, pp. 1932-1940, Dec. 2018.

[15] Q. Ouyang, J. Chen, J. Zheng *et al*., "SOC estimation-based quasi-sliding mode control for cell balancing in lithium-ion battery packs," *IEEE Transactions on Industrial Electronics*, vol. 65, no. 4, pp. 3427-3436, Apr. 2018.

[16] T. R. Oliveira, W. W. Silva, and P. F. Donoso-Garcia, "Distributed secondary level control for energy storage management in DC mi-

crogrids," *IEEE Transactions on Smart Grid*, vol. 8, no. 6, pp. 2597-2607, Nov. 2017.
[17] X. Lu, K. Sun, J. M. Guerrero *et al*., "Double-quadrant state-of-charge- based droop control method for distributed energy storage systems in autonomous DC microgrids," *IEEE Transactions on Smart Grid*, vol. 6, no. 1, pp. 147-157, Jan. 2015.
[18] T. Morstyn, B. Hredzak, and V. G. Agelidis, "Control strategies for microgrids with distributed energy storage systems: an overview," *IEEE Transactions on Smart Grid*, vol. 9, no. 4, pp. 3652-3666, Jul. 2018.
[19] Y. Fu, Z. Zhang, Y. Mi *et al*., "Droop control for DC multi-microgrids based on local adaptive fuzzy approach and global power allocation correction," *IEEE Transactions on Smart Grid*, vol. 10, no. 5, pp. 5468-5478, Sept. 2019.
[20] R. Bhosale and V. Agarwal, "Fuzzy logic control of the ultracapacitor interface for enhanced transient response and voltage stability of a DC microgrid," *IEEE Transactions on Industry Applications*, vol. 55, no. 1, pp. 712-720, Jan. 2019.
[21] M. Farrokhabadi, S. König, K. Bhattacharya *et al*., "Battery energy storage system models for microgrid stability analysis and dynamic simulation," *IEEE Transactions on Power Systems*, vol. 33, no. 2, pp. 2301-2312, Mar. 2018.
[22] Á. Ortega and F. Milano, "Generalized model of VSC-based energy storage systems for transient stability analysis," *IEEE Transactions on Power Systems*, vol. 31, no. 5, pp. 3369-3380, Sept. 2016.
[23] D. Bazargan, S. Filizadeh, and A. M. Gole, "Stability analysis of converter-connected battery energy storage systems in the grid," *IEEE Transactions on Sustainable Energy*, vol. 5, no. 4, pp. 1204-1212, Oct. 2014.
[24] N. Rashidirad, M. Hamzeh, K. Sheshyekani *et al*., "A simplified equivalent model for the analysis of low-frequency stability of multi-bus DC microgrids," *IEEE Transactions on Smart Grid*, vol. 9, no. 6, pp. 6170-6182, Nov. 2018.
[25] S. Kotra and M. K. Mishra, "Design and stability analysis of DC microgrid with hybrid energy storage system," *IEEE Transactions on Sustainable Energy*, vol. 10, no. 3, pp. 1603-1612, Jul. 2021.
[26] W. Xie, M. Han, W. Cao *et al*., "System-level large-signal stability analysis of droop-controlled DC microgrids," *IEEE Transactions on Power Electronics*, vol. 36, no. 4, pp. 4224-4236, Apr. 2021.
[27] S. Bacha, I. Munteanu, and A. I. Bratcu, *Power Electronic Converters Modeling and Control*. London: Springer, 2013.
[28] F. Perez, A. Iovine, G. Damm *et al*., "Stability analysis of a DC microgrid for a smart railway station integrating renewable sources," *IEEE Transactions on Control Systems Technology*, vol. 28, no. 5, pp. 1802-1816, Sept. 2020.
[29] N. L. Diaz, J. C. Vasquez, J. M. Guerrero *et al*., "Intelligent distributed generation and storage units for DC microgrids – a new concept on cooperative control without communications beyond droop control," *IEEE Transactions on Smart Grid*, vol. 5, no. 5, pp. 2476-2485, Sept. 2014.
[30] Y. Gui, R. Han, J. M. Guerrero *et al*., "Large-signal stability improvement of DC-DC converters in DC microgrid," *IEEE Transactions on Energy Conversion*, vol. 36, no. 3, pp. 2534-2544, Sept. 2021.
[31] A. Hosseinipour and H. Hojabri, "Small-signal stability analysis and active damping control of DC microgrids integrated with distributed electric springs," *IEEE Transactions on Smart Grid*, vol. 11, no. 5, pp. 3737-3747, Sept. 2020.
[32] X. Liu, Y. Wang, P. Lin *et al*., "Distributed supervisory secondary control for a DC microgrid," *IEEE Transactions on Energy Conversion*, vol. 35, no. 4, pp. 1736-1746, Dec. 2020.
[33] A. Khodamoradi, G. Liu, P. Mattavelli *et al*., "Analysis of an online stability monitoring approach for DC microgrid power converters," *IEEE Transactions on Power Electronics*, vol. 34, no. 5, pp. 4794-4806, May 2019.
[34] X. Yang, Y. Zhang, H. He *et al*., "Real-time demand side management for a microgrid considering uncertainties," *IEEE Transactions on Smart Grid*, vol. 10, no. 3, pp. 3401-3414, Apr. 2019.
[35] M. K. K. Prince, M. T. Arif, A. Gargoom *et al*., "Modeling, parameter measurement, and control of PMSG-based grid-connected wind energy conversion system," *Journal of Modern Power Systems and Clean Energy*, vol. 9, no. 5, pp. 1054-1065, Sept. 2021.
[36] J. Gu, L. Xie, X. Yang *et al*., "Fuzzy piecewise coordinated control and stability analysis of the photovoltaic-storage direct current microgrid," *IET Renewable Power Generation*, vol. 16, no. 15, pp. 1-14, Aug. 2022.
[37] A. C. Braitor, G. C. Konstantopoulos, and V. Kadirkamanathan, "Current-limiting droop control design and stability analysis for paralleled boost converters in DC microgrids," *IEEE Transactions on Control Systems Technology*, vol. 29, no. 1, pp. 385-394, Jan. 2021.
[38] J. Kim and B. H. Cho, "State-of-charge estimation and state-of-health prediction of a li-ion degraded battery based on an EKF combined with a per-unit system," *IEEE Transactions on Vehicular Technology*, vol. 60, no. 9, pp. 4249-4260, Nov. 2011.
[39] M. O. Qays, Y. Buswig, M. L. Hossain *et al*., "Recent progress and future trends on the state of charge estimation methods to improve battery-storage efficiency: a review," *CSEE Journal of Power and Energy Systems*, vol. 8, no. 1, pp. 105-114, Jan. 2022.
[40] D. Zhai, A. Lu, J. Dong *et al*., "Stability analysis and state feedback control of continuous-time T-S fuzzy systems via anew switched fuzzy Lyapunov function approach," *Applied Mathematics and Computation*, vol. 239, no. 15, pp. 586-599, Aug. 2017.
[41] H. K. Lam and J. Lauber, "Membership-function-dependent stability analysis of fuzzy-model-based control systems using fuzzy Lyapunov functions," *Information Sciences*, vol. 232, no. 20, pp. 253-266, Jan. 2013.

Jipeng Gu received the B.Eng. degree in measurement and control technology and instruments from Longdong University, Qingyang, China, in 2017, and the M. Eng. degree in computer system architecture from Northwest Minzu University, Lanzhou, China, in 2020. He is currently pursuing the Ph. D. degree in control science and engineering at Zhejiang University of Technology, Hangzhou, China. His research interests include smart grid and new energy generation technology, modeling and control of complex systems, fuzzy logic control, and distributed energy storage system.

Xiaodong Yang received the B.S. degree in electrical engineering from Zhejiang A&F University, Hangzhou, China, in 2012, and the Ph. D. degree in control science and engineering from the Zhejiang University of Technology, Hangzhou, China, in 2019. From 2017 to 2019, he was a joint Ph.D. student with the Department of Electrical, Computer, and Biomedical Engineering, University of Rhode Island, Kingston, USA. From 2019 to 2021, he was a Postdoctoral Research Fellow with the Huazhong University of Science and Technology, Wuhan, China. He is currently an Associate Professor with the School of Electrical Engineering and Automation, Hefei University of Technology, Hefei, China. His research interests include resilient distribution system, multi-microgrid system, demand response, and power system control and optimization.

Youbing Zhang received the B.S. and M.S. degrees in electrical engineering from Hunan University, Changsha, China, in 1993 and 1996, respectively, and the Ph.D. degree in electrical engineering from Huazhong University of Science and Technology, Wuhan, China, in 2003. From 1996 to 1997, he was a Research Assistant both at Tsinghua University, Beijing, China, and China Electric Power Research Institute, Beijing, China. From 1997 to 1999, he was a Lecturer at the Department of Electrical Engineering in Hunan University. From 2003 to 2005, he was a Postdoctoral Research Fellow at the Zhejiang University, Hangzhou, China. He is currently a Professor with the College of Information Engineering, Zhejiang University of Technology, Hangzhou, China. His research interests include demand-side management, vehicle-to-grid technology, power quality monitoring and control, smart energy, and big data applications.

Luyao Xie received the B.S. and the Ph.D. degrees in electrical engineering from Beijing Jiaotong University, Beijing, China, in 2007, and 2013, respectively. He is currently an Associate Professor with the Department of Information Engineering, Zhejiang University of Technology, Hangzhou, China. His research interests include power electronics and applications in wind turbines, photovoltaic systems, and battery energy storage systems.

Licheng Wang received the B. Eng. degree in electrical engineering from Huazhong University of Science and Technology (HUST), Wuhan, China, in 2012, the M.Eng degree in electrical engineering from Zhejiang University, Hangzhou, China, in 2015, and the Ph. D. degree in electrical engineering from the University of Queensland, Brisbane, Australia, in 2019. Currently, he is a Tenured Associate Professor in College of Information Engineering, Zhejiang University of Technology, Hangzhou, China. His research interests include power system operation and control, distributed algorithms, renewable energy integration into distribution systems, deep reinforcement learning and its application in networked systems.

Wenwei Zhou received the B.E. and M.E. degrees in instrumentation science and technology from Chonqing University, Chongqing, China, in 2000

and 2003, respectively, and the Ph.D. degree in control theory and control engineering from Zhejiang University of Technology (ZJUT), Hangzhou, China, in 2019. Currently he is a Lecturer at ZJUT. His research interests include power electronics, new energy generation, and electric vehicle charging.

Xiaohui Ge received the B.Eng. and Ph.D. degrees in electrical engineering from Zhejiang University, Hangzhou, China, in 2002 and 2007, respectively. Currently, she is working in Electric Power Research Institute of State Grid Zhejiang Electric Power Co., Ltd., Hangzhou, China. Her research interests include power system operation and control, deep reinforcement learning and its application in networked systems.